Chemical Science

ROYAL SOCIETY OF CHEMISTRY

REVIEW

View Article Online
View Journal | View Issue



Cite this: *Chem. Sci.*, 2026, **17**, 5351

# Integrating efficient and tailored perovskite and organic solar cells into performance-improved tandem photovoltaics

Lu Liu,[ac] Xiaofeng Huang*[bc] and Alex K.-Y. Jen *[abc]

Over the past decade, the certified power conversion efficiency of champion single-junction perovskite solar cells (PSCs) has exceeded 27%. To overcome the theoretical limitation, various perovskite-based tandem solar cells have emerged. Among them, integrating wide bandgap (WBG) perovskites with organic materials in tandem architectures offers a promising avenue toward higher performance while maintaining the advantages of solution processability, high throughput and compatibility with flexible substrates. Perovskite/organic tandem solar cells (POTSCs) employ a two-subcell structure that maximizes spectral utilization; however, achieving high efficiency requires fine control over energy losses, electrical properties, and optical management. In particular, as the top subcells, WBG PSCs absorb high-energy photons and contribute to a high open-circuit voltage ($V_{OC}$), making the minimization of bandgap-$V_{OC}$ losses—through suppression of defect-induced nonradiative recombination—especially critical. The organic rear cell extends absorption into the near-infrared region, enabling sufficient photon harvesting and current matching between the two subcells. The interconnecting layer (ICL), which provides ohmic contact and facilitates efficient carrier recombination between subcells, also requires continued optimization of both its recombination mechanism and interfacial processes. In this review, we first summarize strategies for improving bulk perovskites and interfacial layers, followed by key design principles for ICLs. We then discuss electrical regulation and optical management in organic subcells. Finally, we outline the current challenges and future perspectives of POTSCs to guide the development of high-performance, scalable and flexible tandem photovoltaic technologies.

Received 6th January 2026
Accepted 12th February 2026

DOI: 10.1039/d6sc00127k

rsc.li/chemical-science



## 1. Introduction

Solar energy stands as one of the most promising sustainable and renewable resources, offering an unparalleled abundance: the solar radiation incident on earth exceeds global annual energy consumption by several orders of magnitude. Its availability further enables widespread and decentralized energy deployment.[1] Harnessing this vast resource requires the advancement of high-performance, cost-effective photovoltaic (PV) technologies. Perovskite solar cells (PSCs) have emerged as a transformative technology within the PV community due to their remarkable properties, including broad and tunable absorption (bandgap ~ 1.2–3.0 eV),[2] long charge-carrier diffusion lengths that support efficient charge collection even in micrometer-thick films,[3] facile solution processability suitable for high-throughput manufacturing,[4] and inherent material

[a]*Department of Materials Science and Engineering, City University of Hong Kong, Kowloon 999077, Hong Kong, China. E-mail: alexjen@cityu.edu.hk*
[b]*Department of Chemistry, City University of Hong Kong, Kowloon 999077, Hong Kong, China. E-mail: xhuan7@cityu.edu.hk*
[c]*Hong Kong Institute for Clean Energy, City University of Hong Kong, Kowloon 999077, Hong Kong, China*

*Lu Liu received her B.S. degree in 2018 from Lanzhou University. In 2024, she received her PhD degree under the supervision of Professor Shengzhong Liu at Dalian Institute of Chemical Physics, Chinese Academy of Sciences. Then, she joined City University of Hong Kong as a postdoctoral scholar under the guidance of Professor Alex K.-Y. Jen. Her research interest is mainly focused on perovskite quantum dots, wide-bandgap perovskites and tandem solar cells.*

*Xiaofeng Huang received his B.S. degree in 2017 from Huaqiao University. In 2023, he completed his PhD at Xiamen University under the supervision of Professors Nanfeng Zheng and Binghui Wu. He then joined City University of Hong Kong as a postdoctoral scholar under the guidance of Professor Alex K.-Y. Jen. His research focuses on chemical engineering and materials science related to perovskite photovoltaics.*

defect tolerance.[5] Furthermore, PSCs can be fabricated on flexible substrates, opening avenues for wearable and lightweight PV applications.[6]

The power conversion efficiency (PCE) of small-size single-junction PSCs has skyrocketed from 3.8% in 2009 to a record 27.32% in 2025,[7] approaching the Shockley–Queisser (S–Q) limit of ~33% for an ideal band gap ($E_g$) of 1.34 eV under AM 1.5G illumination.[8] This remarkable progress primarily stems from synergistic advances in perovskite bulk growth control[9] and interface engineering.[10,11] Meanwhile, the long-term device durability has been improved through engineering of the individual functional layers and their relevant interfaces,[12] including the perovskite absorber,[10,13] electron transport layer (ETL), hole transport layer (HTL),[14,15] counter electrode and encapsulation layer. To further boost PCE, researchers have increasingly turned to tandem solar cells (TSCs), a groundbreaking solution to overcome the fundamental efficiency limit of single-junction devices, with theoretical efficiencies exceeding 46%.[16] Tandem architectures combining two or more solar cells with different absorption onsets could collectively capture a broader range of the solar spectrum, minimizing energy loss due to thermalization and transmission (Fig. 1a).[17] Typically, wide-bandgap (WBG) perovskite absorbers (typically 1.6–1.9 eV) are ideal candidates for the top subcell due to their strong absorption in the visible spectrum. Over the past 3–5 years, the PCEs of WBG PSCs with various bandgaps have been significantly enhanced (Fig. 1b). Moreover, they are compatible with a range of narrow-gap (1.2–1.4 eV) subcells, such as organic, silicon, copper–indium–gallium selenide (CIGS), and narrow-bandgap perovskite subcells, which can efficiently harvest near-infrared (NIR) photons as the bottom subcells.[18] Each tandem combination involves its own respective advantages and challenges.[19] Among them, silicon solar cells are the mainstream products of the PV market,[20] and the perovskite/silicon TSCs achieved a rapid rise in efficiency, increasing from 14.3% in 2015 and to over 34% in recent reports.[21–23] However, silicon and perovskite PVs rely on fundamentally different fabrication systems, which increases equipment and manufacturing costs. Moreover, depositing high-quality perovskite films onto industrially textured silicon substrates remains technically challenging. All-perovskite TSCs have reached promising efficiencies exceeding 30%,[24] but these tandem devices suffer from significant stability issues. Particularly, the unfavorable oxidation of $Sn^{2+}$ to $Sn^{4+}$ in tin-lead narrow-gap materials ($E_g$ < 1.3 eV), commonly used as bottom subcells, will induce unintended p-type doping and consequently degrade overall device performance.[25] Though CIGS-based materials have demonstrated flexibility, stability and scalability, their use is limited by complex material synthesis, process sensitivity, and resource constraints.[26]

Narrow-gap organic solar cells (OSCs) have been extensively studied for tandem configurations since the early 2000s.[27] OSCs with absorption spectra extending well into the infrared pose several advantages, including abundant material availability, tunable molecular design, solution processability with environmentally benign solvents, lightweight characteristics, and compatibility with high-throughput fabrication.[28] In addition, their strong NIR absorption coefficient makes them excellent candidates for bottom subcells,[29] enabling significantly reduced thickness (~0.1 μm) compared with Sn/Pb perovskites (~1.2 μm) and CIGS inorganic absorbers (~2.2 μm) in TSC applications. Driven by the continuous development of high-performance novel materials, advances in device fabrication technologies, and a deepened fundamental understanding of both active-layer morphology and device operation mechanisms, OSCs have witnessed rapid development in recent years, with single-junction device efficiencies approaching 21%, especially shown in the fill factor (FF) and open-circuit voltage ($V_{OC}$) improvement (Fig. 1c).[30] Unlike conventional silicon-based tandem structures, organic–inorganic hybrid perovskite and organic materials can be processed using low-energy, solution-based methods compatible with flexible substrates. Techniques such as inkjet printing, blade coating, and slot-die coating techniques have shown strong potential for fabricating large-area perovskite and organic films with high uniformity and reproducibility.[31,32] Through persistent research efforts in WBG PSCs, OSCs and interconnecting layers (ICLs), especially the discovery of Y6-series non-fullerene acceptors (NFAs), the efficiency of lab-scale perovskite–organic tandem solar cells (POTSCs) has increased from below 17% to exceeding 27% (Fig. 1d).[33] Reviewing this progress is therefore valuable for guiding further advancements in POTSC applications.

In this review, we first reviewed recent progress in WBG perovskite subcells, focusing on defect-related nonradiative recombination and phase stability in both the perovskite bulk and at interfaces. We also summarized the strategies for optimizing OSC performance through both electrical regulation and optical management. In addition, to highlight the most critical factors for performance improvement, we discuss the role and requirements of ICLs in tandem devices. Importantly, we spotlight the key issues of combining these two emerging thin-film photovoltaic technologies into a monolithic tandem device. Finally, we outline the specific challenges and opportunities of POTSCs for guiding the development of next-generation high-performance photovoltaic technologies.

*Alex K.-Y. Jen received his B.S. from the National Tsing Hua University in Taiwan and his PhD from the University of Pennsylvania. He served as the Boeing-Johnson Chair Professor and Chair of the Department of Materials Science & Engineering at the University of Washington, Seattle. He was also appointed as Chief Scientist for the Clean Energy Institute endowed by the Washington State Governor. He joined CityU and served as the Provost during 2016–2020. Currently he is the Lee Shau Kee Chair Professor of Materials Science and Director of the Hong Kong Institute for Clean Energy of CityU. He was elected as an Academician by both the European Academy of Sciences and the Washington State Academy of Sciences. He is also a Fellow of several professional societies, including AAAS, MRS, ACS, PMSE, OSA, and SPIE. His research interest focuses on molecular engineering in photonics, optoelectronics, nanomedicine, and nanotechnology.*

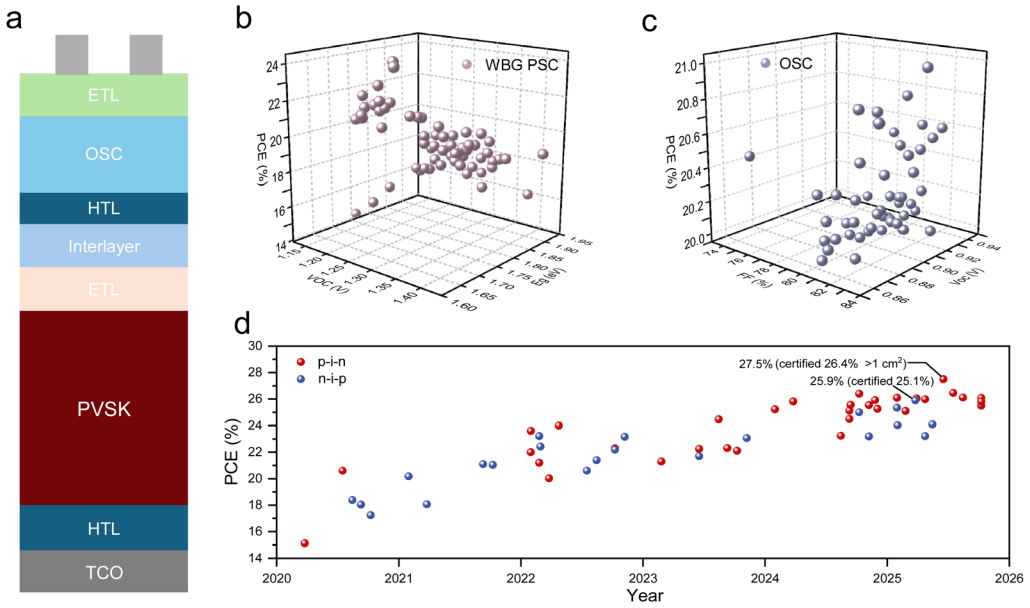


Fig. 1 (a) Schematic illustration of a classical POTSC architecture. PCE development of (b) WBG PSCs, (c) NBG OSCs, and (d) POTSCs with both p–i–n and n–i–p architectures. The corresponding references are provided in SI Tables 1–3, respectively.

## 2. Configuration of TSCs

The relationship between the number of subcells with ideal bandgaps and corresponding theoretical efficiency is presented in Fig. 2a. In theory, a two-subcell tandem device can reach a maximum efficiency of 46% under standard solar spectrum and intensity, while an infinite-junction system would reach 68% efficiency.[34,35] However, considering the increased complexity of fabrication, parasitic absorption and additional costs induced by each extra junction,[36] two-subcell architectures remain the predominant design for tandem devices. According to the connection method, TSCs are classified as monolithic or mechanically stacked, which differ fundamentally in both electrical characteristics and structural design.

Take two-junction for example (Fig. 2b): a monolithic two-terminal (2T) tandem structure consists of a narrow-bandgap bottom subcell directly stacked with a wide-bandgap top subcell, forming an integrated optoelectronic stack. The $V_{OC}$ value of the tandem devices is primarily determined by the sum of the subcells' voltages, neglecting losses introduced by the interconnecting layer, while the short-circuit current ($J_{SC}$) is mainly limited by the lower photocurrent of the two subcells. Therefore, current matching between the top and bottom subcells is essential due to their series-connected architecture. In this regard, theoretical calculations indicate that the PCE of POTSCs is maximized when a WBG (~1.75 eV) perovskite top cell is paired with a NBG (~1.15 eV) organic bottom cell.[37] However, the limited compositional tunability and bandgap control of available active layers typically hinder the realization of this optimal bandgap matching in tandem architectures. The 2T architecture also needs sophisticated charge-collection design, as carriers must transit the entire device stack to reach the electrodes, typically achieved using thin tunnel junctions as ICLs. Conversely, four-terminal (4T) tandem solar cells eliminate the need for current matching requirements as the subcells operate electrically independently (Fig. 2c). This decoupled architecture enables independent optimization of each subcell's efficiency. However, 4T devices require at least one transparent intermediate electrode that ensures high infrared-photon transmission to the bottom subcell. They also

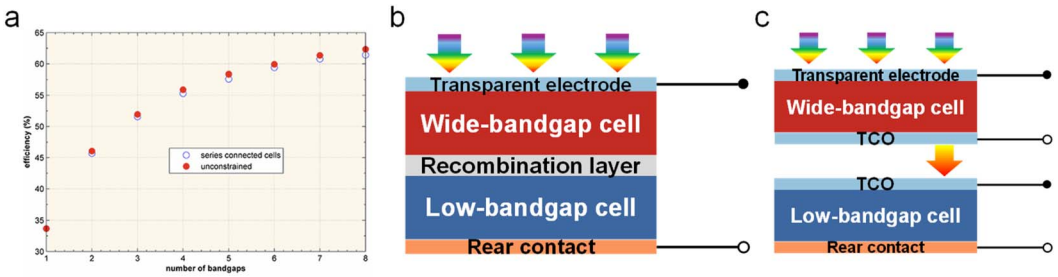


Fig. 2 (a) The ideal laminated cell depends on the number of bandgaps under AM 1.5G illumination. Unconstrained: multiple junctions within the solar cell stack operate independently, each at its own maximum power point (MPP). Copyright Xidian University Press 2021. Schematic diagram of the configuration of (b) 2T and (c) 4T POTSCs. TCO: transparent conductive oxide.

suffer from inherent disadvantages such as increased balance-of-system costs due to separate components and additional parasitic absorption. Considering their operational simplicity, compatibility, and structural integrity, most studies focus on 2T POTSCs, which are the primary subject of the following discussion.

## 3. Optimization for WBG perovskites

As the critical front absorber in POTSCs, WBG perovskites mainly absorb light in the 300–700 nm range,[38,39] requiring precise compositional tuning to achieve an optimal bandgap while maintaining structural stability under high-energy photon exposure. Encouragingly, perovskite materials with the general formula $ABX_3$ exhibit good tunability as semiconductors. In photovoltaic applications, the A-site is commonly occupied by organic cations (*e.g.*, methylammonium, $MA^+$; formamidinium, $FA^+$) or inorganic cations (*e.g.*, $Cs^+$), the B-site predominantly by $Pb^{2+}$ and $Sn^{2+}$, and the X-site by halide anions ($I^-$, $Br^-$, $Cl^-$).[40] It's acknowledged that the bandgap can be regulated by partially substituting iodide with bromide at the X-site of the perovskite lattice.[41] A minimum of 30% of the iodide ions must be replaced by bromide ions to achieve optimal bandgaps of 1.7 and 1.9 eV for the front cell in POTSCs.[42] In principle, increasing the bromide content improves structural stability due to the stronger Pb–Br bond compared to Pb–I bond, stemming from the smaller ionic radius (1.96 Å *vs.* 2.20 Å) and higher electronegativity of $Br^-$ relative to $I^-$.[43] However, the $V_{OC}$ of mixed-halide (I/Br) WBG PSCs does not increase proportionally with bandgap, primarily due to interfacial recombination and the low radiative efficiency of the mixed-halide phase, as well as partially improper energy alignment arising from bromine-rich and iodine-rich domains.[44] Consequently, WBG PSCs display a large $V_{OC}$ deficit (defined as $E_g/q - V_{OC}$), typically ~100 mV higher than that of medium-bandgap PSCs.[45] These shortcomings negatively affect both the performance and operational stability of single-junction WBG devices and POTSCs.

Based on the above discussion, the key challenges to achieving high-performance WBG PSCs are simultaneously mitigating the substantial $V_{OC}$ deficits and stabilizing the perovskite phase. Phase segregation arises from intrinsic composition inhomogeneity and localized strain generated by the interaction between photogenerated carriers and lattice ions, which is further facilitated under light, thermal and electrical stress. In parallel, the $V_{OC}$ deficit originates from nonradiative recombination within the Br-rich absorber and at its interfaces.[46,47] In recent years, researchers have advanced WBG PSC development through various strategies, including composition engineering, additive engineering, interface optimization and improved charge transport layers. In the following parts, we discuss the relevant strategies for POTSC applications.

### 3.1 Composition engineering

Wide-bandgap perovskites are typically based on either all-inorganic $Cs^+$ compositions or organic–inorganic hybrids, with the former possessing superior intrinsic thermal stability.[48] Tan *et al.* introduced a highly polar dipole layer at the all inorganic perovskite $(CsPb(I_xBr_{1-x})_3)/C_{60}$ interface, which reconfigured interfacial states, optimized band alignment, and strengthened the interaction between the inorganic perovskite and the organic contact layers.[49] The resulting all-inorganic perovskite device ($E_g$ = 1.77 eV) yielded a PCE of 18.5%, with a $V_{OC}$ of 1.23 V and average FF > 83%. The devices also demonstrated good reproducibility, with a PCE of 17.3 ± 0.49%. Alex *et al.* further advanced all-inorganic WBG perovskites by incorporating multifunctional additives, 9,10-anthraquinone-2-sulfonic acid and organic cations, to regulate crystallization, achieving a $V_{OC}$ of 1.30 V in single-junction WBG perovskites ($E_g$ = 1.78 eV) and over 23% PCE in integrated POTSC.[50]

Although all-inorganic WBG perovskites exhibit excellent thermal stability, they suffer from significant phase instability, often requiring the partial incorporation of volatile organic cations during film preparation to stabilize the inorganic framework. Consequently, organic–inorganic hybrid perovskites remain the preferred WBG absorbers for tandem devices. Thermodynamically stable MA-based WBG perovskites have been well developed,[51] and incorporating small amounts of $FA^+$ into an MA-based mixed-halide perovskite improves precursor solubility and promotes more homogeneous crystallization.[52] This approach enables the formation of large grains with $PbI_2$ at grain boundaries, where the $PbI_2$ effectively passivates defects and improves film quality ($E_g$ = 1.72 eV). The desired surface trap passivation yielded a champion device with a PCE of 17.4% with $V_{OC}$ of 1.19 V and FF of 78.4%. Moreover, this film-modification strategy thus enabled POTSCs comprising an efficient infrared-absorbing non-fullerene acceptor to attain a PCE of 21.2%. FA-based WBG perovskites offer stronger light absorption but suffer from lattice distortion and phase instability due to the lattice mismatch between A-site cations and the metal–halide framework. To maintain lattice tolerance while preserving thermal stability, partial substitution of FA with $Cs^+$ has been widely adopted. Zhang *et al.* fabricated $FA_{0.5}Cs_{0.5}PbI_3$ films by a hot-flow-assisted spin-coating approach under ambient air conditions with a relative humidity of 50 ± 5%.[53] With an acidic diammonium salt inhibiting the growth of undesired 1D intermediates, an HTL-free carbon electrode-based WBG PSC achieved a PCE of 18.52%, being the highest value reported at that time.

Beyond A-site engineering, X-site modification is also crucial for enhancing the performance of WBG PSCs and POTSCs. The low formation energy of halogen vacancies increases the lattice defect density and promotes halide phase migration.[54] To suppress this segregation, Zhang *et al.* incorporated trace amounts of pseudo-halogen thiocyanate (SCN) ions into a 1.83 eV WBG perovskite ($FA_{0.8}Cs_{0.2}PbI_{1.6}Br_{1.4}$).[55] The SCN ions effectively occupied halide vacancies and retarded halide phase segregation *via* steric hindrance. Ultimately, the formed I/Br/SCN alloy reduced the $V_{OC}$ deficit by 50 mV and improved the PCE of the WBG PSC from 16.97 to 18.96%. The corresponding POTSCs presented PCEs of 25.82% (certified 25.06%; 0.0580 $cm^2$) and 24.45% (1.004 $cm^2$). The tandem devices also showed a high average PCE of 25.34% and a narrow distribution.

Predominantly, both the single-junction and tandem devices demonstrated excellent operational stability, exhibiting a $T_{90}$ exceeding 1000 h under MPP tracking.

### 3.2 Additive engineering

The rapid crystallization kinetics in WBG perovskites induced by high $Cs^+/Br^-$ content often leads to a film with decreasing crystallinity, rough morphology, and a high density of trap states, ultimately contributing to $V_{OC}$ deficit.[56] Also, mixed-halide perovskites often undergo phase separation into I-rich and Br-rich domains due to the low migration activation energy of halide anions. The ion migration is readily triggered under operational stresses such as continuous illumination and heating, thereby severely compromising long-term device durability. Additive engineering has therefore emerged as a key strategy for modulating crystallization for homogeneous compositional distribution, while simultaneously enabling effective defect passivation and structural stabilization.

In general, additive containing functional groups can regulate nucleation and crystallization through their interactions with perovskite precursors and additive/solvent species. An *et al.* proposed a general strategy to manage the crystallization process of WBG perovskites with bandgaps > 1.7 eV.[57] They introduced phenylethylammonium acetate (PEAAc) additive, which contains both amine ($-NH_3^+$) and carboxyl ($-COO^-$) functional groups, into the $FA_{0.8}MA_{0.1}Cs_{0.1}Pb(I_{1-x}Br_x)_3$ ($x = 0.3$–$0.6$) system with bandgaps of 1.73, 1.79, 1.85, and 1.92 eV (Fig. 3a). The multifunctional additive balanced the crystallization kinetics of mixed-halide WBG perovskites by forming both hydrogen-bonding and coordination interactions (Fig. 3b). Ultimately, WBG PSCs with various bandgaps all exhibited high performance, and the corresponding POTSC achieved a stabilized PCE above 24% with a high $V_{OC}$ of 2.197 V (Fig. 3c). In addition, Wang *et al.* prepared a WBG PSC *via* partially replacing dimethyl sulfoxide (DMSO) with 1,3-dimethyl-3,4,5,6-tetrahydro-2(1*H*)-pyrimidinone (DMPU) to regulate the crystallization process.[58] DMPU possessed strong interaction with $PbI_2$, enabling controlled perovskite nucleation and grain growth while continuously releasing $PbI_2$, thereby widening the antisolvent processing window. Benefiting from the improved film quality by solvent engineering, both the performance and stability of the PSCs were enhanced.

Organic cations have also been incorporated into WBG PSCs to passivate bulk defects. Qin *et al.* introduced the organic cation chloroformamidine ($ClFA^+$) into $FA_{0.6}MA_{0.4}Pb(I_{0.6}Br_{0.4})_3$ ($E_g = 1.73$ eV), and the chlorine atom in $ClFA^+$ could partially

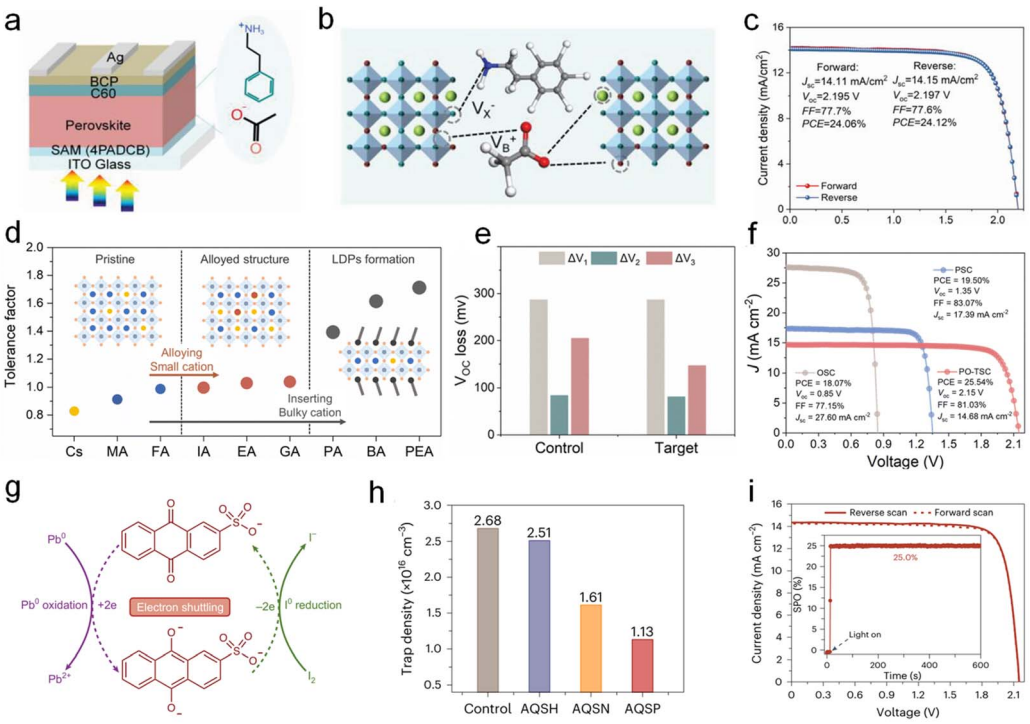


Fig. 3 (a) Application of the PEAAc additive in a WBG p–i–n PSC. (b) Schematic diagram of the interaction between PEAAc and perovskite. (c) *J*–*V* curves of the champion POTSC under forward and reverse scans.[57] Copyright 2023, Wiley-VCH. (d) Tolerance factor and illustration of the corresponding perovskite structure based on the cations' radii. MA (methyl ammonium), FA (formamidinium), IA (imidazolium), EA (ethyl ammonium), GA (guanidinium), PA (propyl ammonium), BA (butyl ammonium) and PEA (phenylethyl ammonium). (e) Analysis of $V_{OC}$ loss for devices with and without the IA additive. $\Delta V_1$: $V_{OC}$ loss due to black-body radiation and non-ideal external quantum efficiency (EQE) above $E_g$. $\Delta V_2$: $V_{OC}$ loss arising from additional thermal radiation in regions where the EQE extends below $E_g$. $\Delta V_3$: $V_{OC}$ loss caused by the non-radiative recombination within the device. (f) *J*–*V* curves of the champion PSC, OSC and POTSC.[59] (g) Electron shuttling between AQS, Pb and I species. (h) The calculated trap density of devices with different AQS derivatives. (i) *J*–*V* curves of the champion POTSC under forward and reverse scans.[60] Copyright 2024, Springer Nature.

compensate for the missing iodine atoms and stabilize excess lead cations.[37] Through iodine defect management, this additive facilitates the formation of high-quality mixed-halide WBG perovskite films, enabling the champion WBG PSC to realize a $V_{OC}$ of 1.25 V and a high FF of 83.0%. To solve the issue that bulky organic ligands often impair charge transport and extraction, imidazolium (IA), which features an aromatic framework and an ideal ionic radius, was incorporated as an A-site alloying cation in the WBG perovskite lattice (Fig. 3d).[59] The introduction of IA balanced the crystallization rate of $I^-$ and $Br^-$ components through electrostatic and coordination interactions, enabling a homogeneous halide distribution in the bulk film. Additionally, the IA cation acts as both a Lewis base and acid to passivate positively and negatively charged defects, leading to superior film quality. In this manner, the optimized 1.79 eV-WBG PSC achieved a PCE of 19.50% with a $V_{OC}$ of 1.35 V, presenting a low energy loss of 0.44 eV, while the monolithic POTSC showed a PCE of 25.54% (Fig. 3e and f). An average PCE of 24.94% was achieved for the tandem devices, demonstrating excellent consistency across the devices.

Especially, building on the critical role of redox shuttles in dye-sensitized solar cells, Jen *et al.* also designed a series of organic mediators with a 2-sulfonate anthraquinone (AQS) core as a redox shuttle to selectively reduce iodine ($I_2$) and oxidize metallic $Pb^0$ (Fig. 3g).[60] The introduction of ammonium ($NH_4^+$) and phenylethyl ammonium ($PEA^+$) groups in place of $H^+$ on the cationic component endowed these molecules with additional defect-passivation capability (Fig. 3h). Consequently, the monolithic POTSCs achieved a high PCE of 25.22% (certified 24.27%), with a high $V_{OC}$ of 2.151 V, $J_{SC}$ of 14.36 mA $cm^{-2}$ and FF of 81.65%, while exhibiting negligible hysteresis (Fig. 3i). Owing to the durable redox-mediated perovskite stabilization, the resultant POTSC retained 92% of its initial PCE after 500 h of continuous operation.

### 3.3 Interface engineering

Given that numerous defects are generated at the film surface, interface engineering is essential for both hybrid and all-inorganic wide-bandgap PSCs. Meanwhile, appropriate interface modification could improve carrier extraction by optimizing the energy-level alignment, further enhancing the device performance.

Organic ammonium halide salts, such as phenmethylammonium chloride[61] and trimethylammonium chloride, have been adopted to modify the perovskite surface.[62] The reconstructed surface effectively reduces defect density while maintaining high uniformity, promoting the growth of a high-quality ICL and enhancing carrier extraction in the monolithic POTSC. Thereby, these POTSCs possess near-ideal $V_{OC}$ superposition, well-matched photocurrent contribution, and high PCE. Besides, a mixed-cation additive strategy, with a combination of 4-trifluoro phenethylammonium ($CF_3$–$PEA^+$, denoted as $CA^+$) and ethylenediammonium ($EDA^{2+}$, denoted as $EA^{2+}$), was utilized to comprehensively regulate structural defects associated with A-, B- and X-sites in WBG perovskite surfaces (Fig. 4a).[63] The complementary passivation reduced the nonradiative recombination rate from 0.80 to 0.11 $ns^{-1}$ and lowered electron/hole defect densities (Fig. 4b and c). The passivated 1.85 eV WBG PSC realized a record $V_{OC}$ of 1.35 V and a high FF of 83.29%. When combined with a quaternary organic bulk-heterojunction, the corresponding POTSC delivered a PCE of 24.47%, with a $V_{OC}$ of 2.14 V, $J_{SC}$ of 14.17 mA $cm^{-2}$ and FF of 80.71%. To confirm the reproducibility, an average PCE of 24.04% with a narrow distribution was calculated from 20 individual tandem cells. Also, the POTSCs exhibited high photothermal stability, maintaining over 90% of the initial PCE after 500 h of MPP tracking.

Typically, passivation layers incorporated at the bottom interface of the perovskite serve a dual role: suppressing interfacial defects and enhancing perovskite crystallization. For example, to address the high defect density in $NiO_x$, Chen *et al.* deposited a benzylphosphonic acid (BPA) layer at the $NiO_x$/perovskite interface (Fig. 4d).[64] This strategy increased the PCE of the WBG PSC from 15.53% to 17.80%, with $V_{OC}$ rising from 1.18 to 1.26 V. When applied in a POTSC, the passivation layer enabled a PCE of 23.6%. Brinkmann *et al.* used MeO–2PACz as the passivation layer to improve the perovskite phase purity and crystallinity.[65] Based on a 1.85 eV perovskite film, the optimal POTSC achieved a high PCE of 24.0% (certified 23.1%) with a high $V_{OC}$ of 2.15 V. To further reinforce the corner-shared $[PbI_6]^{4-}$, Huang *et al.* developed redox-active polyoxometalates (POMs) with ammonium cations, forming a robust polyoxometalate/perovskite interlayer for stabilizing the perovskite phase.[66] Functional POMs not only repair $Pb^0$- and $I^0$-rich defects in $[PbI_6]^{4-}$ framework by electroactive metal ions but also passivate interfacial defects through ammonium cations (Fig. 4e and f). When applied to single-junction 1.78 eV WBG PSCs, the POM-based devices exhibited higher PCEs of 19.75% compared to 18.61% for the control devices. In a POTSC comprising a 1.78 eV perovskite top subcell and a 1.38 eV organic bottom subcell, this approach enabled a remarkable PCE of 24.86%.

In addition to the top- and bottom-interface engineering, dual-interface strategies were developed. Sun *et al.* reported an ionic liquid methylammonium formate (MAFm) to modify the bottom and top interfaces of all-inorganic WBG $CsPbI_2Br$ films.[67] By forming Pb–Fm bonds (Fig. 4g), MAFm-based buried-interface engineering modulated perovskite crystallization and reconstructed the surface morphology, while top-surface engineering effectively passivated defects, yielding uniform films with large grains and a markedly reduced interfacial defect density (Fig. 4h).

## 4. Optimization for interconnecting layers

Typically, an ICL is typically composed of a HTL, ETL, and a thin intermediate metal or metal-oxide carrier recombination layers (Ag, Au, IZO, ITO, AZO, *etc.*).[68] As an essential part of the 2T monolithic tandem solar cells, ICLs not only bridge the top and bottom subcells but also modulate carrier transport and recombination, critically influencing the FF, $J_{SC}$ and $V_{OC}$ of

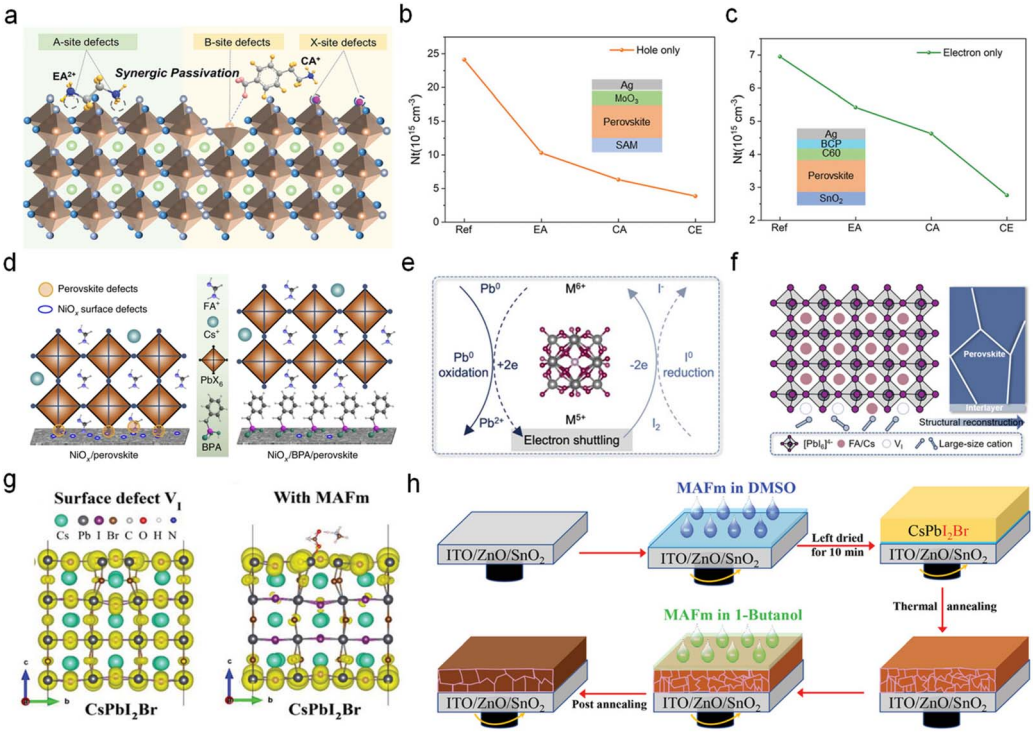


Fig. 4 (a) Schematic illustration of defect passivation in WBG perovskites using CA and EA. Defect densities of the perovskite without and with different passivators based on (b) hole-only devices and (c) electron-only devices, respectively.[63] Copyright 2023, Wiley-VCH. (d) Schematic of BPA passivation on $NiO_x$ HTLs.[64] Copyright 2022, Springer Nature. (e) POM-mediated electron shuttling process between $Pb^0$ and $I^0$. (f) Schematic of the POM-passivated buried surface in perovskite films.[66] Copyright 2024, Wiley-VCH. (g) Partial charge density of $CsPbI_2Br$ with surface defects $V_I$ (Pb–Pb dimer), and the corresponding MAFm-passivated surface defects. (h) Schematic illustration of the dual-interface engineering in the perovskite.[67] Copyright 2023, Wiley-VCH.

TSCs. The parasitic absorption of the ICL could lead to an unbalanced light distribution. Together with interfacial defects at its contact with the active layers, this effect reduced the $V_{OC}$ of the tandem device.[69,70] An ideal ICL should therefore combine high electrical conductivity and chemical inertness to ensure durable ohmic contact formation and efficient inter-subcell carrier recombination, thus minimizing $V_{OC}$ losses, while simultaneously maintaining excellent optical transparency to enable sufficient light transmission to the narrow-bandgap (NBG) bottom subcell for optimal current matching. Additionally, the efficacy of ICLs in balancing carriers between subcells is highly dependent on the thickness of its individual layers, which can be assessed by the relative EQE of each subcell.[71]

To render the interconnect ohmic, thin metals (1 nm Ag or Au) deposited by thermal evaporation are commonly combined with organic/inorganic charge transport layers as ICLs.[72] Chen *et al.* demonstrated that incorporating Ag nanoparticles into $C_{60}$/bathocuproine (BCP)/metal/$MoO_x$ ICLs (Fig. 5a) effectively mitigates efficiency losses caused by energy-level misalignment and promotes balanced, efficient carrier recombination (Fig. 5b).[73] Based on the optimized, all-thermally evaporated, low-loss ICLs, a record PCE of 20.6% was achieved for p–i–n monolithic POTSC, with well-matched $J_{SC}$ between the two subcells (Fig. 5c). To gain balanced carrier transport, An *et al.* proposed a sandwich-structured ICL consisting of $SnO_x$/Au/SAM/$MoO_x$/SAM, in which self-assembled monolayers (SAMs) are anchored to both the top and bottom surfaces of $MoO_x$ (Fig. 5d).[74] Hydrogen bonding and coordination interactions between $MoO_x$ and SAM facilitated a stable, electrically favorable interlayer, while the SAM simultaneously functioned as an electron-blocking layer that reduced interfacial nonradiative recombination (Fig. 5e). This balanced charge transportation enabled the fabricated POTSC to deliver a PCE of 26.05% with excellent current matching (Fig. 5f) and a high $V_{OC}$ of 2.21 V (certified 2.216 V). In addition, the charge-transport material within the ICL plays a critical role in determining device efficiency. Wang *et al.* showed that polyTPD exhibits low parasitic absorption, suitable carrier mobility, and quasi-ohmic contact with adjacent ICL components, facilitating efficient extraction of photogenerated charges, suppressing interfacial charge accumulation and voltage loss, and yielding a remarkably small tandem open-circuit voltage loss of 0.06 V.[75]

Nevertheless, the thin metal-based ICLs can incur substantial optical losses due to parasitic absorption and reflection, as well as challenges in morphology control and potential nanoparticle aggregation. To address the problem, metal oxides with high conductivity, structural stability, and good NIR transmittance have emerged as promising alternative ICL candidates. Hou *et al.* demonstrated a novel ICL architecture comprising a BCP layer, a 4 nm-thick indium zinc oxide (IZO) layer, and a $MoO_x$ layer (Fig. 5g).[64] Compared with the thin Ag layer, sputtered IZO-based ICLs exhibit excellent NIR

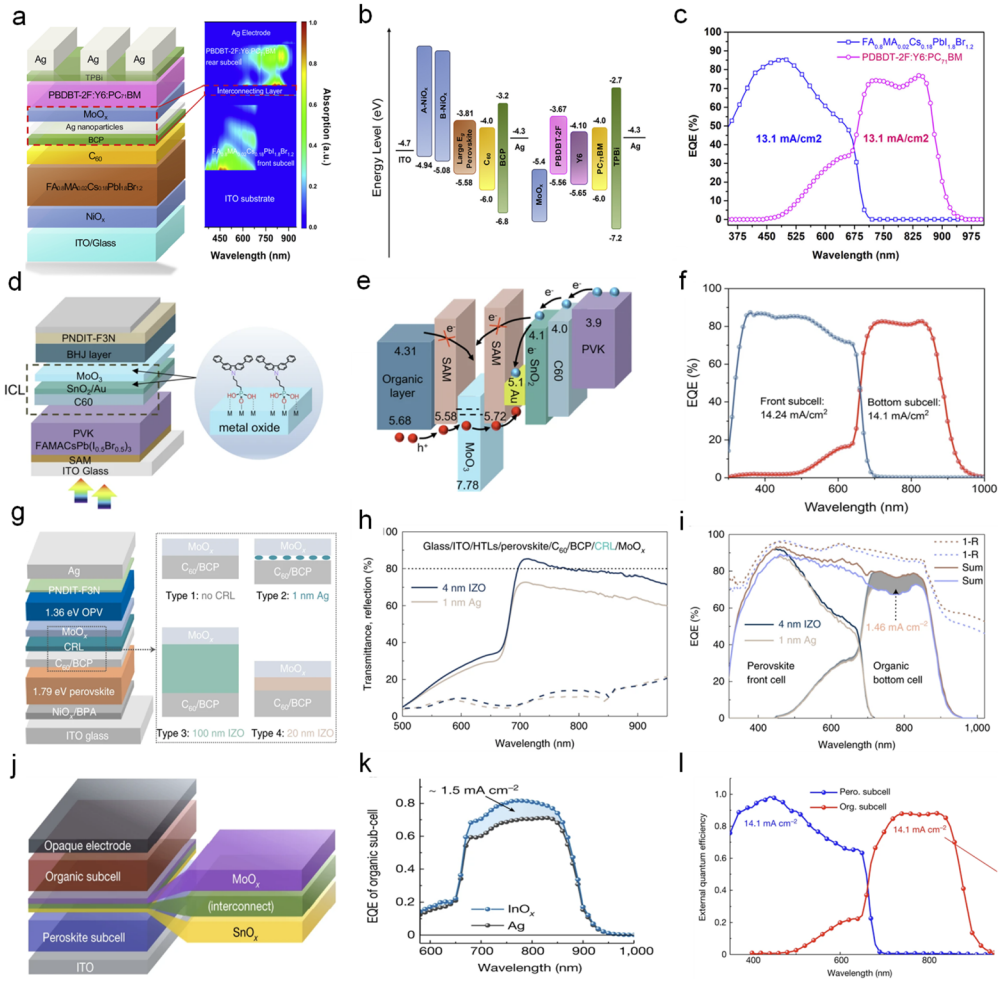


Fig. 5 (a) Schematic diagram of the tandem cell structure highlighting the ICL design and (b) the corresponding energy levels. (c) EQE spectra of POTSCs.[73] Copyright 2020, Elsevier. (d) Schematic diagram of the POTSC structure with the ICL highlighted and (e) associated carrier transport pathways using a $SnO_2$/Au/SAM/$MoO_x$/SAM ICL. (f) EQE spectra of the perovskite and organic subcells.[74] Copyright 2025, Springer Nature. (g) Schematic of the POTSC incorporating the designed ICL. (h) Transmittance spectra of perovskite subcells with 4 nm IZO-based and 1 nm Ag-based ICLs. (i) EQE spectra of TSCs with IZO- and Ag-based ICLs.[64] Copyright 2022, Springer Nature. (j) Schematic diagram of a POTSC with an interconnect. (k) EQE spectra of the organic bottom subcell with $InO_x$ or Ag as an interconnect. (l) EQE spectra of both subcells in the tandem cell.[65] Copyright 2022, Springer Nature.

transmittance, which significantly reduces current losses in the organic bottom subcell (Fig. 5h and i). Furthermore, the thin IZO layer achieved optimized surface coverage, providing abundant recombination sites that facilitate effective charge recombination. By collectively enhancing electrical properties and NIR transparency, the POTSCs reached a certified efficiency of 22.95% (23.60% lab-recorded), along with a $V_{OC}$ of 2.06 V and a $J_{SC}$ of 14.87 mA $cm^{-2}$. Furthermore, the efficiency was well maintained at 21.77% for a larger active area of 1.05 $cm^2$. Besides, Riedl's group developed an ICL with an atomic layer deposition (ALD)-deposited $InO_x$ layer, precisely controlling the thickness to about 1.5 nm.[65] The insertion of amorphous and continuous $InO_x$ enabled barrier-free transport of electrons from the WBG PSCs across the $SnO_x$/$InO_x$/$MoO_x$ layer sequence (Fig. 5j) while reducing optical losses compared to 1 nm Ag (Fig. 5k). Leveraging these advances, $InO_x$-based ICLs delivered an efficiency of 24.0% (certified 23.1%) with a high $V_{OC}$ of 2.15 V and over 1000 h storage stability (Fig. 5l).

## 5. Optimization for organic subcells

In OSCs, excitons efficiently diffuse to the donor–acceptor (D–A) interface, where they dissociate into free charges driven by the internal electric field arising from the lowest unoccupied molecular orbital (LUMO) or highest occupied molecular orbital (HOMO) energy offset between the donor and acceptor. In series-connected POTSCs, the bottom OSC subcell must provide a sufficiently high $V_{OC}$ while maintaining a current output comparable to that of the top PSC subcell. Consequently, the intrinsic properties of the active-layer materials, including donor–acceptor connectivity, domain size, and vertical component distribution, collectively influence exciton dissociation and charge transport, ultimately determining overall device

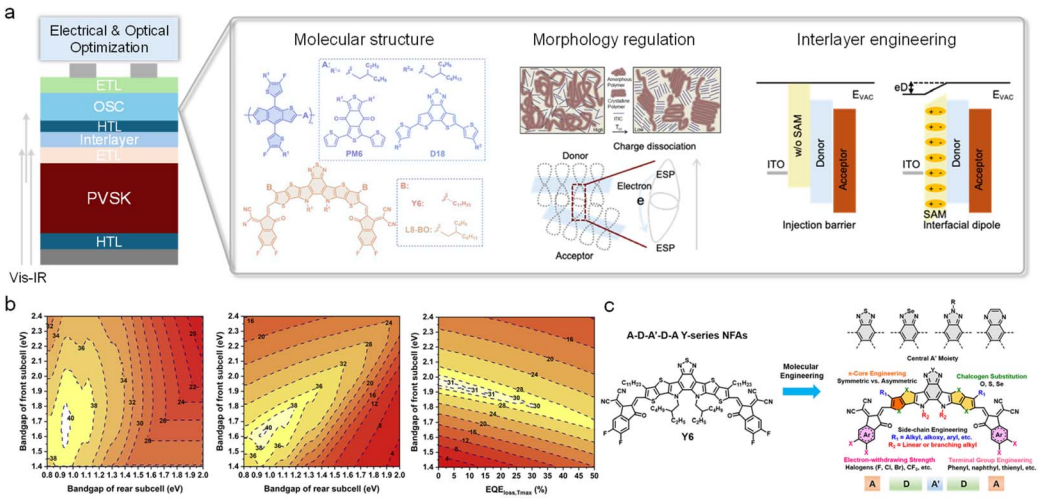


Fig. 6 (a) Roadmap for OSC optimization in POTSCs. (b) S–Q limit for two-junction solar cells with 2-terminal and 4-terminal configurations.[73] Copyright 2020, Elsevier. (c) Structure of the A–DA′D–A-type Y6 and the associated molecular engineering strategies.[76] Copyright 2022, American Chemical Society.

performance, particularly the $V_{OC}$ and $J_{SC}$ contributions in tandem configurations (Fig. 6a).

Furthermore, the bottom OSC subcell must effectively utilize optical energy, particularly in the NIR region, to maximize the integrated current and achieve optimal matching with the top perovskite subcell. A semiempirical model indicates that a PSC with a 1.95 eV bandgap is theoretically optimal for pairing with a Y6-series subcell (Fig. 6b).[73] However, achieving such a high-performance WBG PSC remains challenging due to significant $V_{OC}$ losses. Bandgaps in the range of 1.77–1.83 eV are commonly adopted to minimize $V_{OC}$ loss. Under these conditions, the organic subcell faces increased demands arising from the need for complete and efficient spectral absorption, a lower bandgap, and higher photocurrent generation. To meet these requirements, multi-component active layers and efficient, selective near-infrared absorption by the acceptor are essential. In this section, we summarize primary strategies for optimizing OSCs and related POTSCs from both electrical and optical perspectives. These include molecular structure design, morphological regulation, and interfacial engineering (Fig. 6c).[76] Relevant approaches applied to both single-junction and tandem OSCs are also discussed.

### 5.1 Molecular engineering for optical optimization

Organic semiconductors inherently exhibit quantum-like behavior and vibrational absorption within a defined spectral range. By fine-tuning their molecular structures, both the absorption spectrum and self-assembly characteristics can be effectively tailored. Accordingly, extensive molecular engineering strategies, such as alkyl chain modification, asymmetric core and terminal group design, and heteroatom substitution, have been developed to optimize optical properties. In POTSCs, the bottom OSC subcell must primarily contribute current in the low-energy spectral region, making the acceptor's spectral response particularly critical.

Fused-ring electron acceptors, typically featuring an A–D–A architecture with an electron-donating fused ladder-type core flanked by two electron-accepting end groups, constitute the majority of high-performance non-fullerene acceptors (NFAs). Their molecular frameworks allow versatile structural tailoring to achieve tunable and selective NIR absorption. This is largely governed by intramolecular charge transfer (ICT), driven by the electron push–pull effect between donor and acceptor units (Fig. 7a).[77] Both the ICT pattern and its capacity dictate the absorption characteristics of π-conjugated molecules. For instance, introducing an additional electron-withdrawing unit into the central donor core produces an A–DA′D–A configuration, enabling more precise tuning of absorption and energy levels. Compared with ITIC-type A–D–A NFAs, the A–DA′D–A Y6 family achieves a significantly broader absorption window (900–1000 nm *vs.* 700–800 nm). This improvement arises from inserting a strong electron-withdrawing benzothiadiazole (BT) unit into the core, forming a fused DA′D structure that enhances ICT multiplicity, yielding an absorption onset of ~931 nm. State-of-the-art OSCs now commonly employ Y-series NFAs such as Y6, BTP-eC9, and L8-BO,[78–80] which have also driven performance improvements in POTSCs.

Another effective strategy for enhancing the ICT effect is introducing heteroatoms—such as nitrogen (N) or selenium (Se)—into the fused-ring framework, replacing benzene rings with thiophene units, inserting π-bridges, or extending π-conjugation. For example, substituting an $sp^3$-hybridized carbon with an $sp^2$-hybridized nitrogen allows the nitrogen lone pair on the p-orbital to delocalize into the π-system, thereby strengthening ICT.[81] Likewise, replacing thiophene with selenophene increases polarizability and introduces more delocalized lone-pair electrons, which enhance both intramolecular π-delocalization and intermolecular electron-cloud overlap (Fig. 7b).[82] Owing to the larger atomic size and mass of Se, Se-containing NFAs exhibit stronger intermolecular interactions and improved carrier mobility.[83] Furthermore, the higher

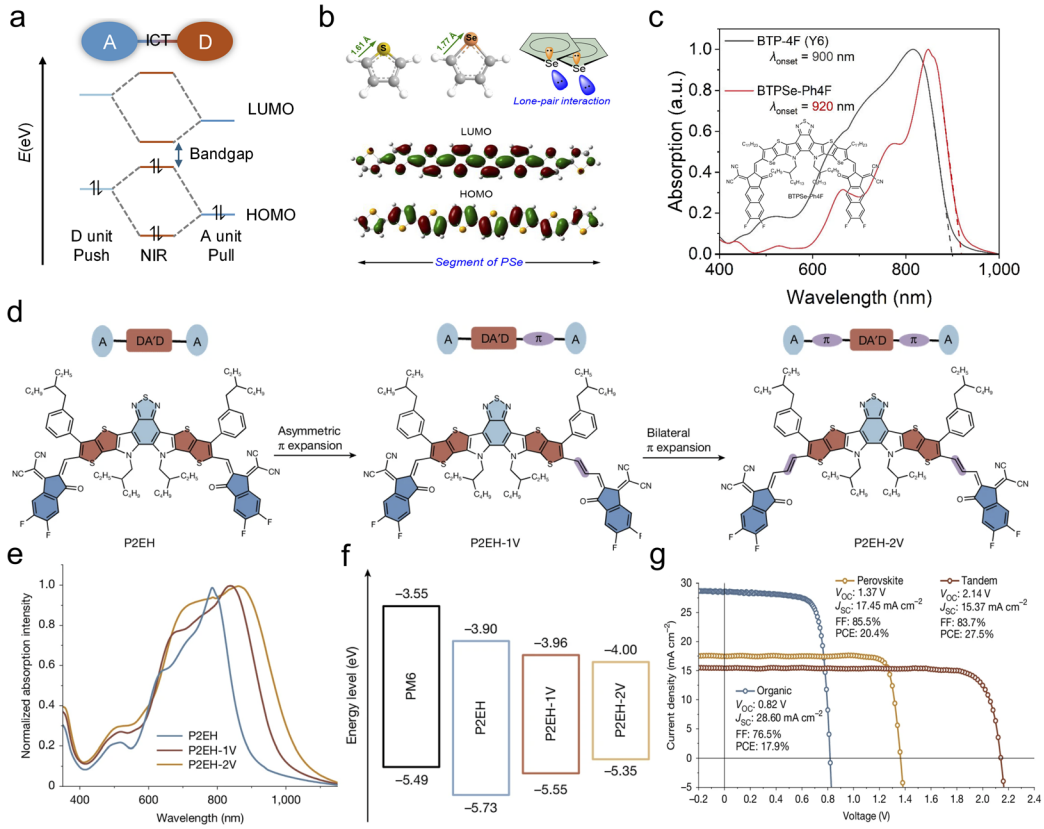


Fig. 7 (a) The design and mechanism of NIR materials.[77] (b) Structural difference between thiophene and selenophene and the corresponding LUMO and HOMO distributions on the polyselenophene backbone (pendant chains omitted).[82] Copyright 2021, American Chemical Society. (c) Chemical structure of BTPSe-Ph4F and its related absorption spectra.[84] Copyright 2021, Springer Nature. (d) Molecular structures of the acceptors incorporating a conjugated π-bridge. (e) Absorption spectra of P2EH, P2EH-1V, and P2EH-2V films. (f) Energy-level diagram of PM6 and the neat acceptor films. (g) Combination of champion *J*–*V* curves and photovoltaic parameters of single-junction OSCs, PSCs and POTSCs.[33] Copyright 2025, Springer Nature.

polarizability and electron-rich nature of selenophene reinforce the quinoidal character and broaden the absorption spectrum.

By combining these structural modifications to optimize both ICT patterns and intensity, acceptors with broadened absorption windows and enhanced charge-transport properties can be achieved. For instance, the A–DA′D–A-type acceptor BTPSe-Ph4F ($E_g$ = 1.27 eV) exhibits a ~20 nm red shift in absorption compared with Y6. When employed as the active layer and optimized to a thickness of 120 nm for pairing with a 1.88 eV WBG PSC, the integrated tandem device achieves a $J_{SC}$ of 15.4 mA cm$^{-2}$ and a PCE of 26.4% (Fig. 7c).[84] A further extension of NIR absorption can be expected with increasing Se substitution.[85] Additionally, ternary organic rear subcells containing two narrow-bandgap NFAs have been designed to further enhance NIR absorption. Using a diffusion-controlled growth method to regulate the ternary morphology significantly improves exciton dissociation efficiency, broadens NIR absorption, and promotes efficient exciton generation and separation.[86]

To further extend absorption, end groups are generally designed as halogenated IC units, while the core structures incorporate extended π-conjugation. For example, inserting an ethylene π-bridge between the end groups and the central core of Y6 increases the conjugation length and broadens the absorption spectrum, leading to the development of the NFA BTPV-4F, which exhibits a red-shifted absorption up to 1021 nm.[87] More recently, the asymmetric NFA P2EH-1V, which incorporates a unilateral conjugated π-bridge, successfully reduced the optical bandgap to 1.27 eV while maintaining efficient exciton dissociation and favorable nanomorphology. This design achieved an efficiency of 17.9% for the organic bottom cell with a high $J_{SC}$ of 28.60 mA cm$^{-2}$, and enabled a record PCE of 26.7% (certified 26.4%) in POTSCs over an aperture area exceeding 1 cm$^2$ (Fig. 7d–g).[33] Another promising direction involves adopting a highly electron-rich dithienopicenocarbazole (DTPC) core derived from perylene to construct the acceptors DTPC-IC and DTPC-DFIC, using IC and 2FIC as end groups, respectively. These acceptors exhibit an absorption onset extending to 1020 nm.[88] Building on these molecular motifs, numerous structural modifications have been implemented to tune ICT intensity, enabling higher current contributions from the organic bottom subcell.

### 5.2 Morphological engineering for electrical optimization

In addition to the development of tailored organic photovoltaic molecules, precise control over microscopic morphology is

crucial for optimizing exciton dissociation and diffusion at D/A interfaces, as well as the frontier molecular orbital energy offsets between the donor and acceptor. An ideal vertical phase morphology features purer domains, longer exciton diffusion lengths, shorter charge-transport pathways, and more efficient charge collection. Numerous studies have shown that the morphology of the active layer depends not only on intrinsic material properties, such as polymer regularity, molecular weight, and donor/acceptor ratio, but also on processing methods, including solvent selection, annealing treatments, and additive engineering (Fig. 8a).

To ensure efficient exciton diffusion and provide sufficient D/A interfacial area for exciton dissociation, an interpenetrating network with continuous donor and acceptor phases is required, making the D/A ratio a critical parameter. Quantitative correlations between key morphological and electrical properties—such as crystallinity, phase separation, and exciton recombination—have shown that an optimized D/A stoichiometry markedly improves exciton dissociation yield and charge-transport efficiency. In contrast, insufficient donor content disrupts molecular ordering in the active layer and consequently degrades device performance (Fig. 8b–d).[89] Equally important is selecting donor materials capable of forming well-organized nanoscale morphologies with suitable domain size and purity to ensure efficient charge transport. For instance, the unique chemical structure of PM6 promotes rope-like domains with dense, ordered molecular packing. Continued molecular design of donor materials will further enable precise morphological control to enhance exciton generation, diffusion, dissociation, and charge transport.

Processing methods are also widely explored. For example, grazing-incidence wide-angle X-ray scattering analysis revealed that the distinct performances of PM6:Y6 OSCs processed using chloroform *versus* chlorobenzene arise from differences in Y6 solubility and molecular crystallinity. Chloroform induces stronger crystallinity in Y6 films, whereas chlorobenzene results in low crystallinity and random molecular orientation (Fig. 8e).[90] Annealing treatments, including solvent-vapor annealing and thermal annealing, can further drive the active-layer morphology toward thermodynamic stability. These processes promote spontaneous crystallization of donor and acceptor molecules, enlarge phase domains, and improve the formation of interpenetrating networks. As a result, exciton dissociation efficiency is enhanced, leading to higher-performance OSC devices.

Additive engineering employs both solvent and solid additives, each influencing film formation through distinct mechanisms. Thermodynamically, additives modulate intra- and intermolecular interactions between donor and acceptor molecules and leverage solubility differences to control phase-separation size and the resulting active-layer morphology. Common solvent additives, such as 1,8-diiodooctane and 1-chloronaphthalene, typically exhibit higher boiling points than the host solvent. Consequently, they evaporate more slowly during film deposition and may remain partially in the blend. Removing these residual additives often requires high-temperature thermal annealing, which can enlarge phase-separation domains and deteriorate device performance, while also negatively affecting the top WBG perovskite subcell.

Kinetic methods regulate solution aggregation, film formation, and post-treatment through the use of additives, enabling precise control over crystallization and phase separation to tailor the final film morphology.[91] The crystallization kinetics of non-fullerene acceptors can be effectively tuned using crystallization-controlling agents such as acenaphthene (AP).[92] This additive directs acceptor self-assembly through a two-step crystallization process: it first fixes the molecular packing motif and then refines the crystalline framework, yielding highly oriented acceptor domains within the active layer. This well-organized morphology provides multiple charge-transport

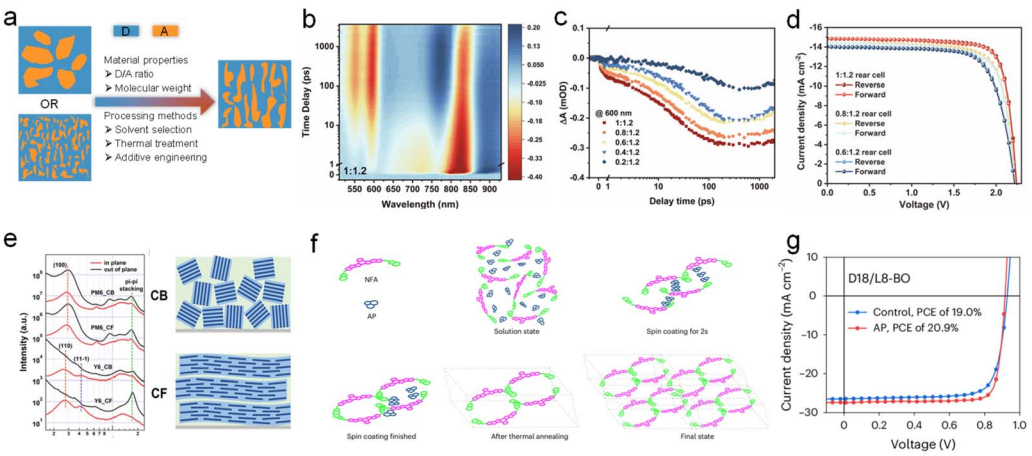


Fig. 8 (a) Morphology regulation strategies for DA blend films. (b) Contour plots of the TA spectra of the D18 : BTP-eC9-4F (1 : 1.2) blend film pumped at 800 nm. (c) TA traces at 600 nm for D18:BTP-eC9-4F blend films with varying D18 content. (d) *J*–*V* curves of POTSCs with different rear subcells.[89] Copyright 2025, Springer Nature. (e) Scattering profiles for pure films of PM6 and Y6 processed with CB and CF and the corresponding arrangement sketch map of molecules in films.[90] Copyright 2020, John Wiley and Sons. (f) Schematic illustration of AP-induced two-step crystallization engineering. (g) *J*–*V* curves of D18/L8-BO OSCs without and with AP processing.[92] Copyright 2025, Springer Nature.

pathways, thereby enhancing device charge-transport properties. As a result, a high PCE of 20.9% (certified 20.4%) was achieved for the D18/L8-BO-based device (Fig. 8f and g). Moreover, the use of solid additives overcomes several limitations associated with solvent additives. Because solid additives remain in the active layer, high-temperature annealing is unnecessary, thereby preventing thermal degradation and improving the stability of both single-junction and tandem devices.

### 5.3 Interfacial regulation for electrical optimization

A high-performance tandem device imposes stringent requirements on the charge-transporting layers, particularly the hole-contact interface, which must provide a dense film with good electrical contact for efficient charge extraction while minimizing optical losses to maximize light harvesting. PEDOT:PSS has been widely employed as a HTL owing to its high conductivity and suitable work function. However, it suffers from intrinsic limitations, including phase separation that generates insulating PSS-rich domains, the risk of damaging the underlying subcell during aqueous processing, and parasitic absorption arising from its relatively low optical bandgap. Metal oxides have also been extensively explored as bottom HTLs in OSCs because of their intrinsic chemical stability; however, their low conductivity and the need for complex deposition or post-treatment processes limit their practical applications. Recently, SAMs have emerged as promising hole-selective layer candidates due to their excellent hole-contact properties and high transmittance across the vis-NIR region, offering a pathway toward more efficient and stable interfacial engineering in OSCs.[93]

To achieve improved interfacial energy-level alignment and complete surface coverage, several strategies, such as molecular design, co-deposition optimization, and SAM compositing, have been developed. For instance, directly incorporating Me–4PACz into the organic precursor solution enables its self-assembly at the $MoO_x$/organic bulk heterojunction (BHJ) interface during solution processing. The resulting enhancement in device performance demonstrates that the *in situ*-formed SAM facilitates efficient charge extraction at the interface while simplifying fabrication (Fig. 9a and b). Although $MoO_x$ possesses a wide bandgap exceeding 3.3 eV, undesired parasitic absorption in the NIR region can still occur when the film thickness increases, particularly in POTSC systems where the subcells exhibit overlapping absorption between 450 and 720 nm. Incorporating Me–4PACz enables the use of a thinner $MoO_x$ layer, thereby minimizing parasitic absorption while maintaining excellent carrier transport properties (Fig. 9c). Consequently, the resultant POTSCs achieve a remarkable PCE of 25.56% (certified: 24.65%) with a record FF of 83.62%.[94] The average PCE of 25.10% and its low standard deviation of ± 0.14% proved the reproducibility of the developed strategies. Compared with a standalone SAM, a co-SAM provides denser and more uniform surface coverage, effectively suppressing

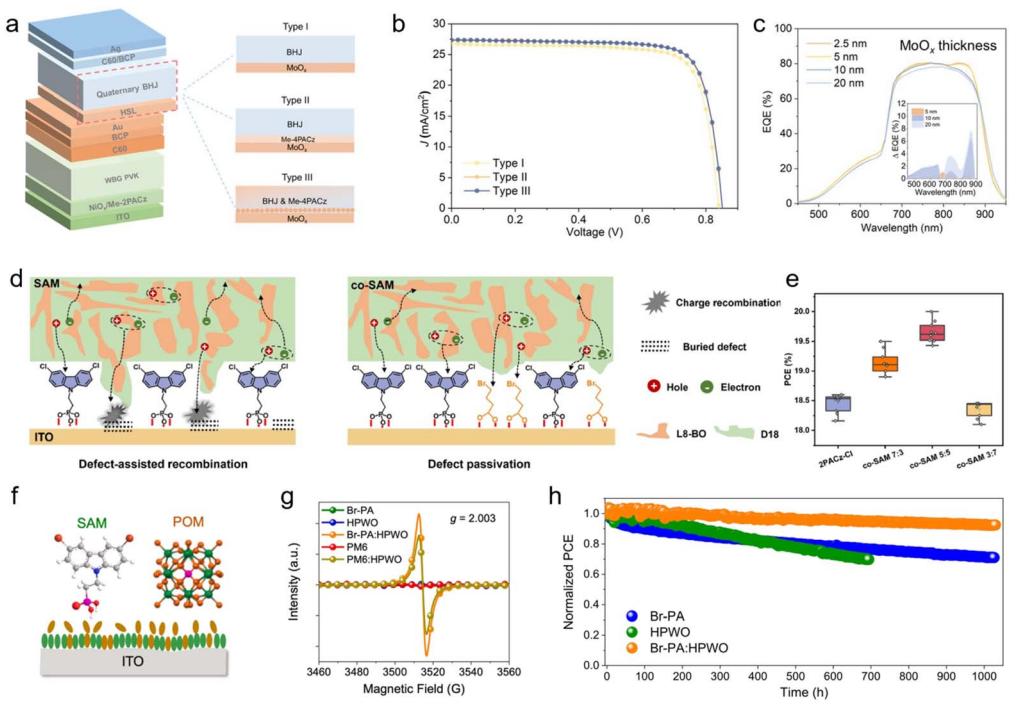


Fig. 9 (a) Device configuration and (b) *J*–*V* curves of the fabricated POTSCs. (c) EQE spectra of POTSCs with different ICLs.[94] Copyright 2024, John Wiley and Sons. (d) Schematic illustration of exciton and charge recombination behaviors at defect-buried *versus* passivated interfaces. (e) PCE statistics of devices with different HTLs.[95] Copyright 2025, Springer Nature. (f) Chemical structures of Br–PA and POM and the configuration of the Br–PA:POM composite in devices. (g) ESR spectra of Br–PA, POM, PM6, and their solid-state blends. (h) MPP tracking of devices with different HTLs under continuous one-sun illumination.[97] Copyright 2024, Elsevier.

interfacial nonradiative recombination. Furthermore, the incorporation of 4-BrAc deepens the work function of the ITO/co-SAM interface, promoting faster hole extraction. As a result, the device achieves a significantly improved PCE of 20.0% (Fig. 9d and e), and an even higher PCE of 25.8% has been achieved in POTSCs.[95]

Achieving a conformally stable SAM substrate in OSCs is also essential for ensuring the long-term stability of POTSCs. A hybrid HTL strategy, combining an ultrathin SAM with a POM, has been developed to improve surface coverage (Fig. 9f) and induce p-doping in the polymer donor,[96] thereby increasing the charge carrier density (Fig. 9g). Consequently, the optimized OSCs with the stabilized SAM:POM composite effectively suppress burn-in decay caused by degradation of the standalone hole-selective layer (Fig. 9h), which can be attributed to the robust ohmic contact at the HTL/active-layer interface during physical aging.[97]

## 6. Summary and perspectives

The emergence of perovskite and organic materials offers a promising path toward performance-improved, cost-effective tandem solar cells. These thin-film photovoltaic materials not only provide complementary optical and electronic properties but also enable innovative device architectures that can be tailored for specific applications, setting the stage for the next generation of high-efficiency photovoltaics. To minimize energy losses arising from intrinsic material properties and the fabrication process of multilayer tandem devices, researchers have dedicated themselves to reducing the defect-induced nonradiative recombination and suppressing mixed-halide-triggered phase separation in WBG PSCs. In parallel, ICL architectures have been optimized to enhance charge transportation and optical transmittance, while organic subcells have undergone electrical and optical optimizations of organic absorbers and interfacial layers. These efforts have enabled POTSCs to achieve a certified PCE of 26.4%. Nevertheless, their performance and research progress still lag behind those of perovskite–silicon and all-perovskite tandem architectures. Concurrently, studies on long-term stability remain limited and insufficient for commercialization requirements, and scaling up to large-area devices remains a significant challenge. Continued advancements in POTSCs are therefore anticipated to address these critical barriers.

(1) In terms of efficiency, a key challenge for POTSCs is their low $J_{SC}$, which stems from the limited photon harvesting of advanced Y6-series NFAs. These NFAs exhibit incomplete visible absorption and restricted NIR extension, resulting in limited external EQE and increased energy loss. To overcome this limitation, it is essential to design novel NFAs with absorption extending beyond 1000 nm in the NIR, complemented by visible-light compensation through third components, while ensuring efficient charge transport and minimal energy loss. The low charge mobility of organic BHJ layers and energy-level misalignment at the perovskite/organic interface induce pronounced charge recombination, significantly reducing the FF and overall PCE. Developing BHJ materials with high carrier mobility and optimizing energy-level alignment are therefore critical for performance enhancement. Furthermore, conventional narrow-bandgap donors often fail to effectively block electrons due to their deep LUMO levels, necessitating molecular-level design of new BHJ systems combining narrow-bandgap acceptors with wide-bandgap donors for improved near-infrared absorption and charge management. Looking ahead, the integration of machine learning with high-throughput techniques could accelerate the discovery of novel organic materials with enhanced photovoltaic properties, optimizing device architectures, and streamlining fabrication processes, thereby potentially reshaping the landscape of POTSC research.[98] Considering that organic subcells haven't yet approached their realistic efficiency limit (currently just above 21%), continued molecular design and interface optimization could enable an additional 2–4% absolute increase in tandem PCE in the coming years.

(2) Regarding stability, both perovskite and organic materials are susceptible to environmental factors such as moisture, UV light, and oxygen. Photoinduced halide segregation is a major degradation pathway in WBG perovskite subcells. This process leads to the formation of iodine-rich, low-bandgap domains, resulting in reduced radiative efficiency, $V_{OC}$ loss, and visible color changes. Mobile ions ($I^-$, $Br^-$, $MA^+$) migrate under bias, illumination, or heat, which not only accelerates halide segregation but also leads to reactions with metal electrodes or charge transport layers, subsequently corroding interfaces. Organic cations ($MA^+$, $FA^+$) can volatilize at elevated temperatures, causing collapse of the perovskite lattice. In narrow-bandgap NFA subcells, chemical bonds are highly susceptible to attack by singlet oxygen generated under light and oxygen exposure. This degrades the molecular backbone, disrupts active-layer morphology, and causes rapid loss of $J_{SC}$. Thermal stress can induce excessive phase separation or crystallization of donor/acceptor domains, impairing charge generation and transport. Additionally, interdiffusion between subcells can accelerate device degradation. Halide ions from the perovskite may diffuse through the ICL and poison the organic active layer, while organic materials from the subcells can reach the recombination layer, inducing significant non-radiative recombination. Therefore, ICLs with structural and electrical stability, as well as dense morphology, are essential to mitigate these effects.

It is acknowledged that OSCs with $T_{95} > 5000$ h under MPP tracking and WBG PSCs with $T_{90} \approx 500$ h after aging at 60 °C in an $N_2$ atmosphere have been reported.[63,65] Furthermore, POTSCs exhibit improved operational stability compared with single OSCs due to the UV filtering by the WBG perovskite subcells, indicating promising long-term stability.[99] However, comprehensive studies on POTSC stability under various International Summit on Organic Photovoltaic Stability (ISOS) protocols remain limited. A deeper understanding of the critical factors affecting tandem stability, including both the absorber and functional layers, is still required. In addition, while advances in component materials facilitate performance, the development of edge-sealed, hermetic encapsulation with water

vapor transmission rates below $10^{-6}$ g per $m^2$ per day is essential for achieving device longevity.

(3) For scalable manufacturing, current solution-processable large-area film deposition methods (*e.g.*, blade coating, spray coating, slot-die printing) still yield inferior film quality compared to spin coating.[100] These challenges are exacerbated at the module level due to increased film inhomogeneity and a higher likelihood of defects in large-area thin films,[101] highlighting to need to narrow the performance gap during device scaling. By increasing the thickness of the OSC layer, Yang's group fabricated a 18.48 $cm^2$-POTSC module achieving a PCE of 18.54% for the first time,[31] and flexible POTSCs have been demonstrated with a PCE of 13.61%.[102] The potential for flexible POTSC modules is further enabled by low-temperature fabrication processes compatible with a roll-to-roll procedure. Thus, in-depth investigation of film formation mechanisms and the development of innovative, industrial-scale fabrication techniques are urgently needed.

From these perspectives, the anticipated improvements in efficiency, stability, and manufacturability position of POTSCs make them promising candidates for applications in wearable electronics, smart windows, and integrated energy-harvesting systems.

## Author contributions

L. L. and X. H. conducted the literature research for the review and contributed to the discussion of the content and writing. X. H. and A. K. Y. J. contributed to the discussion, writing, and editing of the manuscript.

## Conflicts of interest

The authors declare no conflict of interest.

## Data availability

No primary research results, software or code have been included and no new data were generated or analysed as part of this review.

## Acknowledgements

A. K. Y. J. thanks the sponsorship of the Lee Shau-Kee Chair Professor (Materials Science), and the support from the APRC Grants (9380086, 9610419, 9610440, 9610492, 9610508) of the City University of Hong Kong, the MHKJFS Grant (MHP/054/23), TCFS grant (GHP/121/22SZ) and MRP Grant (MRP/040/21X) from the Innovation and Technology Commission of Hong Kong, the Green Tech Fund (202020164) from the Environment and Ecology Bureau of Hong Kong, and the GRF grants (11307621, 11316422, 11308625) and CRS grants (CRS_CityU104/23, CRS_HKUST203/23) from the Research Grants Council of Hong Kong. This work was partially financially supported by City University of Hong Kong (9610739) for the project "Fostering Innovation for Resilience and Sustainable Transformation", officially endorsed by the United Nations Educational, Scientific and Cultural Organization under the International Decade of Sciences for Sustainable Development (2024–2033).

## References

1 Y. Shi, J. J. Berry and F. Zhang, *ACS Energy Lett.*, 2024, **9**, 1305–1330.
2 S. De Wolf, J. Holovsky, S.-J. Moon, P. Löper, B. Niesen, M. Ledinsky, F.-J. Haug, J.-H. Yum and C. Ballif, *J. Phys. Chem. Lett.*, 2014, **5**, 1035–1039.
3 S. D. Stranks, G. E. Eperon, G. Grancini, C. Menelaou, M. J. Alcocer, T. Leijtens, L. M. Herz, A. Petrozza and H. J. Snaith, *Science*, 2013, **342**, 341–344.
4 A. Younis, C. H. Lin, X. Guan, S. Shahrokhi, C. Y. Huang, Y. Wang, T. He, S. Singh, L. Hu and J. R. D. Retamal, *Adv. Mater.*, 2021, **33**, 2005000.
5 Y. Zhao, Q. Zeng, Y. Yu, T. Feng, Y. Zhao, Z. Wang, Y. Li, C. Liu, J. Liu and H. Wei, *Mater. Horiz.*, 2020, **7**, 2719–2725.
6 Y. Hu, T. Niu, Y. Liu, Y. Zhou, Y. Xia, C. Ran, Z. Wu, L. Song, P. Müller-Buschbaum and Y. Chen, *ACS Energy Lett.*, 2021, **6**, 2917–2943.
7 *Best Research-cell Efficiency Chart*, https://www.nrel.gov/pv/cell-efficiency.html.
8 P. Chen, Y. Xiao, S. Li, X. Jia, D. Luo, W. Zhang, H. J. Snaith, Q. Gong and R. Zhu, *Chem. Rev.*, 2024, **124**, 10623–10700.
9 G. Li, Z. Su, L. Canil, D. Hughes, M. H. Aldamasy, J. Dagar, S. Trofimov, L. Wang, W. Zuo and J. J. Jerónimo-Rendon, *Science*, 2023, **379**, 399–403.
10 H. Chen, C. Liu, J. Xu, A. Maxwell, W. Zhou, Y. Yang, Q. Zhou, A. S. Bati, H. Wan and Z. Wang, *Science*, 2024, **384**, 189–193.
11 S. Liu, J. Li, W. Xiao, R. Chen, Z. Sun, Y. Zhang, X. Lei, S. Hu, M. Kober-Czerny and J. Wang, *Nature*, 2024, **632**, 536–542.
12 Q. Li, Y. Zheng, H. Wang, X. Liu, M. Lin, X. Sui, X. Leng, D. Liu, Z. Wei and M. Song, *Science*, 2025, **387**, 1069–1077.
13 R. Nie, Y. Dai, R. Wang, L. Li, B.-w. Park, W. Chu, C. Wang, Z. Li, S. Chen and R. Qiao, *Nat. Commun.*, 2025, **16**, 7343.
14 J. Zhou, L. Tan, Y. Liu, H. Li, X. Liu, M. Li, S. Wang, Y. Zhang, C. Jiang and R. Hua, *Joule*, 2024, **8**, 1691–1706.
15 B. Dong, M. Wei, Y. Li, Y. Yang, W. Ma, Y. Zhang, Y. Ran, M. Cui, Z. Su and Q. Fan, *Nat. Energy*, 2025, **10**, 342–353.
16 H. Li and W. Zhang, *Chem. Rev.*, 2020, **120**, 9835–9950.
17 R. Wang, T. Huang, J. Xue, J. Tong, K. Zhu and Y. Yang, *Nat. Photonics*, 2021, **15**, 411–425.
18 Z. Zhang, Z. Li, L. Meng, S. Y. Lien and P. Gao, *Adv. Funct. Mater.*, 2020, **30**, 2001904.
19 K. O. Brinkmann, P. Wang, F. Lang, W. Li, X. Guo, F. Zimmermann, S. Olthof, D. Neher, Y. Hou and M. Stolterfoht, *Nat. Rev. Mater.*, 2024, **9**, 202–217.
20 Y. Cheng and L. Ding, *SusMat*, 2021, **1**, 324–344.
21 J. P. Mailoa, C. D. Bailie, E. C. Johlin, E. T. Hoke, A. J. Akey, W. H. Nguyen, M. D. McGehee and T. Buonassisi, *Appl. Phys. Lett.*, 2015, **106**, 121105.
22 M. A. Green, K. Emery, Y. Hishikawa, W. Warta and E. D. Dunlop, *Prog. Photovoltaics Res. Appl.*, 2012, **20**, 12–20.

23 F. Fu, J. Li, T. C. J. Yang, H. Liang, A. Faes, Q. Jeangros, C. Ballif and Y. Hou, *Adv. Mater.*, 2022, **34**, 2106540.
24 Z. Liu, R. Lin, M. Wei, M. Yin, P. Wu, M. Li, L. Li, Y. Wang, G. Chen and V. Carnevali, *Nat. Mater.*, 2025, **24**, 252–259.
25 Y. Liu, T. Ma, C. Wang, Z. Yang, Y. Zhao, Z. Wu, C. Chen, Y. Bao, Y. Zhai and T. Jia, *Nat. Commun.*, 2025, **16**, 3477.
26 J. X. Zhai, L. Xie and S. Shafian, *Nanotechnol. Rev.*, 2025, **14**, 20250196.
27 A. Hadipour, B. de Boer and P. W. Blom, *Adv. Funct. Mater.*, 2008, **18**, 169–181.
28 J. Yi, G. Zhang, H. Yu and H. Yan, *Nat. Rev. Mater.*, 2024, **9**, 46–62.
29 A. Sharma, N. Gasparini, A. Markina, S. Karuthedath, J. Gorenflot, H. Xu, J. Han, A. Balawi, W. Liu and D. Bryant, *Adv. Mater.*, 2024, **36**, 2305367.
30 C. Li, Y. Cai, P. Hu, T. Liu, L. Zhu, R. Zeng, F. Han, M. Zhang, M. Zhang and J. Lv, *Nat. Mater.*, 2025, **24**, 1626–1634.
31 X. Chen, Z. Jia, Z. Chen, C. Zhou, S. Huang, X. Xia, S. Liang, P. Wang, T. Jiang, T. Liu, X. Xu, B. Yan, J. Yao, X. Lu, W. Shen, H. Zhu and Y. Yang, *Adv. Mater.*, 2025, **37**, 2500190.
32 X. Hu, C. Zhao, Y. Liu, J. A. Li, L. Wang, X. Tang, Y. Dou, X. Shi, T. Liu and S. Luo, *Adv. Funct. Mater.*, 2025, **36**, e12093.
33 Z. Jia, X. Guo, X. Yin, M. Sun, J. Qiao, X. Jiang, X. Wang, Y. Wang, Z. Dong and Z. Shi, *Nature*, 2025, **643**, 104–110.
34 C. Zhang, J. Zhang, X. Ma and Q. Feng, in *Semiconductor Photovoltaic Cells*, Springer, 2021, pp. 433–461.
35 S. Bremner, M. Levy and C. B. Honsberg, *Prog. Photovoltaics Res. Appl.*, 2008, **16**, 225–233.
36 M. T. Horantner, T. Leijtens, M. E. Ziffer, G. E. Eperon, M. G. Christoforo, M. D. McGehee and H. J. Snaith, *ACS Energy Lett.*, 2017, **2**, 2506–2513.
37 S. Qin, C. Lu, Z. Jia, Y. Wang, S. Li, W. Lai, P. Shi, R. Wang, C. Zhu and J. Du, *Adv. Mater.*, 2022, **34**, 2108829.
38 S. Wu, M. Liu and A. K.-Y. Jen, *Joule*, 2023, **7**, 484–502.
39 G. E. Eperon, M. T. Hörantner and H. J. Snaith, *Nat. Rev. Chem.*, 2017, **1**, 0095.
40 Q. Jiang, J. Tong, R. A. Scheidt, X. Wang, A. E. Louks, Y. Xian, R. Tirawat, A. F. Palmstrom, M. P. Hautzinger and S. P. Harvey, *Science*, 2022, **378**, 1295–1300.
41 H. Shen, D. Walter, Y. Wu, K. C. Fong, D. A. Jacobs, T. Duong, J. Peng, K. Weber, T. P. White and K. R. Catchpole, *Adv. Energy Mater.*, 2020, **10**, 1902840.
42 T. Leijtens, K. A. Bush, R. Prasanna and M. D. McGehee, *Nat. Energy*, 2018, **3**, 828–838.
43 J. Wang, W. Li and W. J. Yin, *Adv. Mater.*, 2020, **32**, 1906115.
44 F. Peña-Camargo, P. Caprioglio, F. Zu, E. Gutierrez-Partida, C. M. Wolff, K. Brinkmann, S. Albrecht, T. Riedl, N. Koch and D. Neher, *ACS Energy Lett.*, 2020, **5**, 2728–2736.
45 A. J. Ramadan, R. D. Oliver, M. B. Johnston and H. J. Snaith, *Nat. Rev. Mater.*, 2023, **8**, 822–838.
46 C. G. Bischak, C. L. Hetherington, H. Wu, S. Aloni, D. F. Ogletree, D. T. Limmer and N. S. Ginsberg, *Nano Lett.*, 2017, **17**, 1028–1033.
47 R. He, S. Ren, C. Chen, Z. Yi, Y. Luo, H. Lai, W. Wang, G. Zeng, X. Hao and Y. Wang, *Energy Environ. Sci.*, 2021, **14**, 5723–5759.
48 J. Wang, J. Zhang, Y. Zhou, H. Liu, Q. Xue, X. Li, C.-C. Chueh, H.-L. Yip, Z. Zhu and A. K. Jen, *Nat. Commun.*, 2020, **11**, 177.
49 T. Li, J. Xu, R. Lin, S. Teale, H. Li, Z. Liu, C. Duan, Q. Zhao, K. Xiao and P. Wu, *Nat. Energy*, 2023, **8**, 610–620.
50 Y. Li, Y. Yan, Y. Fu, W. Jiang, M. Liu, M. Chen, X. Huang, G. Lu, X. Lu and J. Yin, *Angew. Chem., Int. Ed.*, 2024, **63**, e202412515.
51 Y.-M. Xie, C. Ma, X. Xu, M. Li, Y. Ma, J. Wang, H. T. Chandran, C.-S. Lee and S.-W. Tsang, *Nano Res.*, 2019, **12**, 1033–1039.
52 Y. M. Xie, Q. Yao, Z. Zeng, Q. Xue, T. Niu, R. Xia, Y. Cheng, F. Lin, S. W. Tsang and A. K. Y. Jen, *Adv. Funct. Mater.*, 2022, **32**, 2112126.
53 R. Zhang, L. Li, W. Wang, Z. Wu, Y. Wang, J. Hong, H. Rao, Z. Pan and X. Zhong, *Adv. Funct. Mater.*, 2023, **33**, 2300552.
54 Y. Yuan and J. Huang, *Acc. Chem. Res.*, 2016, **49**, 286–293.
55 Z. Zhang, W. Chen, X. Jiang, J. Cao, H. Yang, H. Chen, F. Yang, Y. Shen, H. Yang and Q. Cheng, *Nat. Energy*, 2024, **9**, 592–601.
56 Z. Fang, N. Yan and S. Liu, *InfoMat*, 2022, **4**, e12369.
57 Y. An, N. Zhang, Z. Zeng, Y. Cai, W. Jiang, F. Qi, L. Ke, F. R. Lin, S. W. Tsang and T. Shi, *Adv. Mater.*, 2024, **36**, 2306568.
58 R. Wang, J. Zhu, J. You, H. Huang, Y. Yang, R. Chen, J. Wang, Y. Xu, Z. Gao and J. Chen, *Energy Environ. Sci.*, 2024, **17**, 2662–2669.
59 M. Chen, Y. Li, Z. Zeng, M. Liu, T. Du, X. Huang, L. Bi, J. Wang, W. Jiang and Y. An, *Energy Environ. Sci.*, 2024, **17**, 9580–9589.
60 S. Wu, Y. Yan, J. Yin, K. Jiang, F. Li, Z. Zeng, S.-W. Tsang and A. K.-Y. Jen, *Nat. Energy*, 2024, **9**, 411–421.
61 X. Wu, Y. Liu, F. Qi, F. Lin, H. Fu, K. Jiang, S. Wu, L. Bi, D. Wang and F. Xu, *J. Mater. Chem. A*, 2021, **9**, 19778–19787.
62 W. Chen, D. Li, X. Chen, H. Chen, S. Liu, H. Yang, X. Li, Y. Shen, X. Ou and Y. Yang, *Adv. Funct. Mater.*, 2022, **32**, 2109321.
63 X. Wang, D. Zhang, B. Liu, X. Wu, X. Jiang, S. Zhang, Y. Wang, D. Gao, L. Wang and H. Wang, *Adv. Mater.*, 2023, **35**, 2305946.
64 W. Chen, Y. Zhu, J. Xiu, G. Chen, H. Liang, S. Liu, H. Xue, E. Birgersson, J. W. Ho, X. Qin, J. Lin, R. Ma, T. Liu, Y. He, A. M.-C. Ng, X. Guo, Z. He, H. Yan, A. B. Djurišić and Y. Hou, *Nat. Energy*, 2022, **7**, 229–237.
65 K. Brinkmann, T. Becker, F. Zimmermann, C. Kreusel, T. Gahlmann, M. Theisen, T. Haeger, S. Olthof, C. Tückmantel, M. Günster, T. Maschwitz, F. Göbelsmann, C. Koch, D. Hertel, P. Caprioglio, F. Peña-Camargo, L. Perdigón-Toro, A. Al-Ashouri, L. Merten, A. Hinderhofer, L. Gomell, S. Zhang, F. Schreiber, S. Albrecht, K. Meerholz, D. Neher, M. Stolterfoht and T. Riedl, *Nature*, 2022, **604**, 280–286.
66 X. Huang, L. Bi, Z. Yao, Q. Fu, B. Fan, S. Wu, Z. Su, Q. Feng, J. Wang and Y. Hong, *Adv. Mater.*, 2024, **36**, 2410564.

67 S. Q. Sun, X. Xu, Q. Sun, Q. Yao, Y. Cai, X. Y. Li, Y. L. Xu, W. He, M. Zhu and X. Lv, *Adv. Energy Mater.*, 2023, **13**, 2204347.
68 D. Zhao, C. Chen, C. Wang, M. M. Junda, Z. Song, C. R. Grice, Y. Yu, C. Li, B. Subedi and N. J. Podraza, *Nat. Energy*, 2018, **3**, 1093–1100.
69 Y. M. Xie, Q. Yao, H. L. Yip and Y. Cao, *Small Methods*, 2023, **7**, 2201255.
70 M. De Bastiani, A. S. Subbiah, E. Aydin, F. H. Isikgor, T. G. Allen and S. De Wolf, *Mater. Horiz.*, 2020, **7**, 2791–2809.
71 Y.-M. Xie, T. Niu, Q. Yao, Q. Xue, Z. Zeng, Y. Cheng, H.-L. Yip and Y. Cao, *J. Energy Chem.*, 2022, **71**, 12–19.
72 A. Axelevitch, B. Gorenstein and G. Golan, *Phys. Procedia*, 2012, **32**, 1–13.
73 X. Chen, Z. Jia, Z. Chen, T. Jiang, L. Bai, F. Tao, J. Chen, X. Chen, T. Liu and X. Xu, *Joule*, 2020, **4**, 1594–1606.
74 Y. An, N. Zhang, Q. Liu, W. Jiang, G. Du, D. Chen, M. Liu, X. Huang, T. Lei and Q. Qiu, *Nat. Commun.*, 2025, **16**, 1–11.
75 P. Wang, W. Li, O. J. Sandberg, C. Guo, R. Sun, H. Wang, D. Li, H. Zhang, S. Cheng, D. Liu, J. Min, A. Armin and T. Wang, *Nano Lett.*, 2021, **21**, 7845–7854.
76 G. Zhang, F. R. Lin, F. Qi, T. Heumüller, A. Distler, H.-J. Egelhaaf, N. Li, P. C. Chow, C. J. Brabec and A. K.-Y. Jen, *Chem. Rev.*, 2022, **122**, 14180–14274.
77 J. Zyss, I. Ledoux, S. Volkov, V. Chernyak, S. Mukamel, G. P. Bartholomew and G. C. Bazan, *J. Am. Chem. Soc.*, 2000, **122**, 11956–11962.
78 J. Yuan, Y. Zhang, L. Zhou, G. Zhang, H.-L. Yip, T.-K. Lau, X. Lu, C. Zhu, H. Peng and P. A. Johnson, *Joule*, 2019, **3**, 1140–1151.
79 C. Li, J. Zhou, J. Song, J. Xu, H. Zhang, X. Zhang, J. Guo, L. Zhu, D. Wei and G. Han, *Nat. Energy*, 2021, **6**, 605–613.
80 Y. Cui, H. Yao, J. Zhang, K. Xian, T. Zhang, L. Hong, Y. Wang, Y. Xu, K. Ma and C. An, *Adv. Mater.*, 2020, **32**, 1908205.
81 C. Huang, X. Liao, K. Gao, L. Zuo, F. Lin, X. Shi, C.-Z. Li, H. Liu, X. Li and F. Liu, *Chem. Mater.*, 2018, **30**, 5429–5434.
82 B. Fan, F. Lin, X. Wu, Z. Zhu and A. K.-Y. Jen, *Acc. Chem. Res.*, 2021, **54**, 3906–3916.
83 F. Qi, F. R. Lin and A. K. Y. Jen, *Sol. RRL*, 2022, **6**, 2200156.
84 X. Jiang, S. Qin, L. Meng, G. He, J. Zhang, Y. Wang, Y. Zhu, T. Zou, Y. Gong and Z. Chen, *Nature*, 2024, **635**, 860–866.
85 Q. Fan, H. Fu, Q. Wu, Z. Wu, F. Lin, Z. Zhu, J. Min, H. Y. Woo and A. K. Y. Jen, *Angew. Chem., Int. Ed.*, 2021, **60**, 15935–15943.
86 X. Cui, G. Xie, Y. Liu, X. Xie, H. Zhang, H. Li, P. Cheng, G. Lu, L. Qiu and Z. Bo, *Adv. Mater.*, 2024, **36**, 2408646.
87 B. Brommer, M. He, Z. Zhang, Z. Yang, J. C. Page, J. Su, Y. Zhang, J. Zhu, E. Gouy and J. Tang, *Nat. Commun.*, 2021, **12**, 781.
88 Z. Yao, X. Liao, K. Gao, F. Lin, X. Xu, X. Shi, L. Zuo, F. Liu, Y. Chen and A. K.-Y. Jen, *J. Am. Chem. Soc.*, 2018, **140**, 2054–2057.
89 X. Cui, G. Xie, G. Ran, Y. Liu, X. Ma, G. Zhang, Q. Kong, W. Zhang, H. Li and P. Cheng, *Nat. Commun.*, 2025, **16**, 8986.
90 L. Zhu, M. Zhang, G. Zhou, T. Hao, J. Xu, J. Wang, C. Qiu, N. Prine, J. Ali and W. Feng, *Adv. Energy Mater.*, 2020, **10**, 1904234.
91 Z. Li, X. Kong, Y. Liu, H. Qiu, L. Zhan and S. Yin, *Chin. Chem. Lett.*, 2024, **35**, 109378.
92 J. Fu, H. Li, H. Liu, P. Huang, H. Chen, P. W. Fong, T. A. Dela Peña, M. Li, X. Lu and P. Cheng, *Nat. Energy*, 2025, **10**, 1251–1261.
93 M. Li, M. Liu, F. Qi, F. R. Lin and A. K.-Y. Jen, *Chem. Rev.*, 2024, **124**, 2138–2204.
94 X. Wu, D. Zhang, B. Liu, Y. Wang, X. Wang, Q. Liu, D. Gao, N. Wang, B. Li and L. Wang, *Adv. Mater.*, 2024, **36**, 2410692.
95 X. Ma, Y. Liu, X. Cui, G. Xie, J. Zhang, Y. Ji, R. Deng, C. Cao, W. Cao and W. Huang, *Sci. China Chem.*, 2026, **69**, 813–818.
96 W. Jiang, B. Fan, L. Kong, Z. F. Yao, W. Shang, C. T. Wong, F. R. Lin and A. K. Y. Jen, *Angew. Chem., Int. Ed.*, 2025, **64**, e202507273.
97 B. Fan, H. Gao, Y. Li, Y. Wang, C. Zhao, F. R. Lin and A. K.-Y. Jen, *Joule*, 2024, **8**, 1443–1456.
98 V. de la Asunción-Nadal, C. I. Sprague, B. Guijarro-Berdiñas, U. B. Cappel and A. García-Fernández, *EES Sol.*, 2025, **1**, 927–957.
99 X. Meng, Z. Jia, X. Niu, C. He and Y. Hou, *Nanoscale*, 2024, **16**, 8307–8316.
100 L. Bi, J. Wang, Z. Zeng, X. Ji, X. Huang, F. R. Lin, S.-W. Tsang, Q. Fu and A. K.-Y. Jen, *Nat. Photonics*, 2025, 1–9.
101 S. Chen, X. Dai, S. Xu, H. Jiao, L. Zhao and J. Huang, *Science*, 2021, **373**, 902–907.
102 Z. Li, S. Wu, J. Zhang, K. C. Lee, H. Lei, F. Lin, Z. Wang, Z. Zhu and A. K. Jen, *Adv. Energy Mater.*, 2020, **10**, 2000361.